Inhomogeneous Photosusceptibility of VO_2 Films at the Nanoscale

A. J. Sternbach,[1,*,†] T. Slusar,[3] F. L. Ruta,[1,2] S. Moore,[1] X. Chen,[1,4] M. K. Liu,[4] H. T. Kim,[3] A. J. Millis,[1] R. D. Averitt,[5] and D. N. Basov[1]

[1]*Department of Physics, Columbia University, New York, New York 10027, USA*
[2]*Department of Applied Physics and Applied Mathematics, Columbia University, New York, New York 10027, USA*
[3]*Electronics and Telecommunications Research Institute, Daejeon, 34129 Republic of Korea*
[4]*Department of Physics, Stony Brook University, Stony Brook, New York 11790, USA*
[5]*Department of Physics, University of California San Diego, San Diego, California 92093, USA*

(Received 5 November 2023; accepted 3 April 2024; published 3 May 2024)

Pump-probe nano-optical experiments were used to study the light-induced insulator to metal transition (IMT) in thin films of vanadium dioxide (VO_2), a prototypical correlated electron system. We show that inhomogeneous optical contrast is prompted by spatially uniform photoexcitation, indicating an inhomogeneous photosusceptibility of VO_2. We locally characterize temperature and time dependent variations of the photoexcitation threshold necessary to induce the IMT on picosecond timescales with hundred nanometer spatial resolution. We separately measure the critical temperature T_L, where the IMT onsets and the local transient electronic nano-optical contrast at the nanoscale. Our data reveal variations in the photosusceptibility of VO_2 within nanoscopic regions characterized by the same critical temperature T_L where metallic domains can first nucleate.

DOI: 10.1103/PhysRevLett.132.186903

Light can alter quantum materials. In the case of transition metal oxides, photoexcitation can initiate first-order phase transitions including the insulator-to-metal transition (IMT) in vanadium dioxide (VO_2) [1–8]. The properties of light induced states are often transient and need to be documented on ultrafast femtosecond (fs) and picosecond (ps) timescales [9]. However, inhomogeneous phase separation [10] can complicate the interpretation of experimental data. Recently, a few spatially resolved nano-pump-probe studies have been carried out to address the role of inhomogeneity in the light-induced IMT [7,11–13].

Previous research has established inhomogeneity of the transient conductivity in the light induced IMT of VO_2 [2,5–7,11–14]. The photoexcitation energy is an important parameter of the problem. The IMT in VO_2 can be activated on sub-100 fs timescales, but this process requires relatively high photoexcitation energies [1,3,4,6,15–17]. It is well established that the photoexcitation energy must exceed a threshold to induce the IMT in VO_2 [15,16]. At photoexcitation energies just above threshold, the terahertz optical conductivity increases with a rise time on the order of ∼100 ps, which is much longer than the convolution of the pump and probe pulse durations (∼300 fs) that are typically used in these experiments [2]. The hundred picosecond long rise time has been conjectured to arise from some combination of nucleation and growth [2,5,12]. Within the last decade nano optical experiments have confirmed the notion that the transient conductivity is inhomogeneous [7,11]. The data and analysis in Ref. [12] indicated that natural boundaries, including grain boundaries, can mediate nucleation and provided an estimate of the growth rate. This evidence all confirms the notion that the transient conductivity can be inhomogeneous in the light induced IMT in VO_2.

To visualize and spatially resolve transient metallicity in VO_2, we use time-resolved scattering near-field optical microscopy [2,6,7,11,13,18] (Tr-SNOM). Tr-SNOM measurements [Fig. 1(a)] access the amplitude of optical scattered near fields, S, with spatial resolution defined by the tip radius, $a \approx 20$ nm at a fixed time delay Δt after photoexcitation (see Supplemental Material [19] Sec. 2.1 for experimental details). Metals are characterized by a large, and insulators by a small, low-frequency conductivity. Owing to this difference, and at infrared frequencies well below band gaps, small values of S are observed when the tip is in the near-field of an insulator, while S is much larger when the tip is in the near-field of a metallic surface [28]. In our experiments we use probe radiation with a wavelength of 8 μm, well below the ∼0.7 eV(1.7 μm) band gap of VO_2 and different enough from phonon frequencies that ac conductivity of metallic VO_2 is dominated by the Drude-like response. The values of S observed on metallic VO_2 are comparable to values observed on metals such as gold [29–31]. The contrast of S between metallic and insulating VO_2, therefore, allows us to distinguish these phases locally, with ∼20 nm spatial resolution. Pump-induced increases of the near-field amplitude, ΔS, reveal transient metallicity. The probe beam is vertically polarized (along the tip shaft) while the pump beam is horizontally polarized (perpendicular to the tip

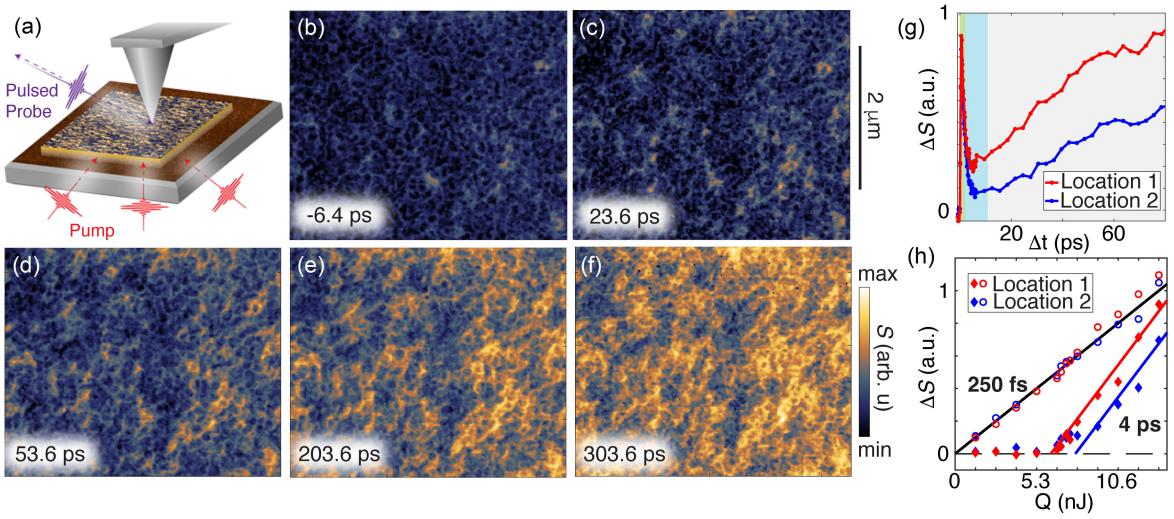

FIG. 1. Nano-optical study of the light induced IMT in a VO_2 film. All data in Fig. 1 were obtained with an initial temperature $T_i = 330$ K. (a) Schematic of the experiment. A horizontally polarized pump beam (red pulses) initiates the IMT. We use a vertically polarized 8 μm wavelength pulsed probe (purple pulse) focused on an AFM tip to monitor the local near-field amplitude, S, at a variable time delay, Δt, after photoexcitation. In our experiments, temperature dependent data is obtained by changing the initial (equilibrium) temperature of the sample, T_i, with a heat stage. (b)–(f), Images of S, using 5.3 nJ of photoexcitation power, obtained (b), before photoexcitation: $\Delta t = -6.4$ ps, and (c)–(f), after photoexcitation: (c) $\Delta t = 23.6$, (d) $\Delta t = 53.6$, (e) $\Delta t = 203.6$, (f) $\Delta t = 303.6$ ps. (g) Dynamics of the pump induced change of the near-field amplitude ΔS obtained at two representative locations, Location 1 and location 2, where values of S are near the extremes of high and low contrast observed in panel (f), respectively. The green, blue, and gray shaded regions mark the first, second, and third stages, respectively, of the three-step response to photoexcitation as described in the main text. (h) Data of ΔS are shown against the photoexcitation energy at the same two locations investigated in panel (g). Data collected at $\Delta t = 250$ fs are shown with open circles, while data obtained at $\Delta t = 4$ ps are shown with filled diamonds. Note that systematic inhomogeneity observed at $\Delta t = 250$ fs and above Q_c likely derives from carriers that have abruptly transitioned to the metallic state (see Supplemental Material [19], Sec. 2.4 for details and discussion).

shaft) to minimize inhomogeneity of the photoexcitation profile (see Supplemental Material [19], Fig. S7). In our experiments, we use an above bandgap pump with a fixed photon-energy, 1.2 eV. The photo-excitation energy per pulse (e.g., the number of 1.2 eV photons) is varied with a motorized attenuator. We place a beam splitter in the pump beam line to simultaneously monitor the photoexcitation energy while the Tr-SNOM signal is also measured. The Tr-SNOM technique offers subpicosecond temporal resolution limited only by the durations of the pump and probe beams [2,6,7,11,13].

Inhomogeneous optical contrast is observed in the data shown in Figs. 1(b)–1(f), which we interpret as arising from inhomogeneous transient metallicity, consistent with prior reports [7,11,12]. At a fixed above threshold photoexcitation energy, dynamics of ΔS show a three-step response to photoexcitation [Fig. 1(g)]. First, ΔS increases on a femtosecond timescale [green region in Fig. 1(g)]. Then, ΔS exhibits a decrease on picosecond timescales [blue region in Fig. 1(g)]. Finally, ΔS shows an inhomogeneous increase with a ~30–100 ps rise time [gray region in Fig. 1(g)]. The first two stages are consistent with electron-hole pair injection (described below) followed by a semiconducting-like relaxation or carrier trapping, in agreement with Refs. [11,15,16]. We interpret the third, inhomogeneous, process as arising from the nucleation and growth of the metallic phase, consistent with prior works [2,5,12].

Our data reveal inhomogeneous photosusceptibility in the regime of uniform photoexcitation [Fig. 1(h)]. Data obtained ~250 fs after photoexcitation are characterized by the trend where a linear increase of ΔS occurs in response to an increase of the photoexcitation energy, Q. Later, at $\Delta t \gtrsim 4$ ps, ΔS increases rapidly only above a certain threshold photoexcitation energy, Q_c. In Fig. 1(h) we investigated two representative locations where the values of Q_c are inhomogeneous. At these same locations, $\Delta S(\Delta t = 250\ \text{fs}, Q < Q_c)$ increases with a spatially uniform slope (differing by <0.02% between the two locations). In our experiments, we utilize an above band gap pump photon-energy, 1.2 eV, which promotes electrons from the $d_{||}$ band, below the Fermi level, to the π conduction band. The number of electron-hole pairs created is expected to be proportional to the number of above-gap pump photons or applied photoexcitation energy. Our observation of a linear increase of ΔS at $\Delta t = 250$ fs is consistent with the notion of linear electron-hole pair injection. Moreover, the observation that $\Delta S(\Delta t = 250\ \text{fs}, Q < Q_c)$ increases with the same linear slope at the two locations indicates that the electron-hole pair injection process is homogeneous, within the error of our

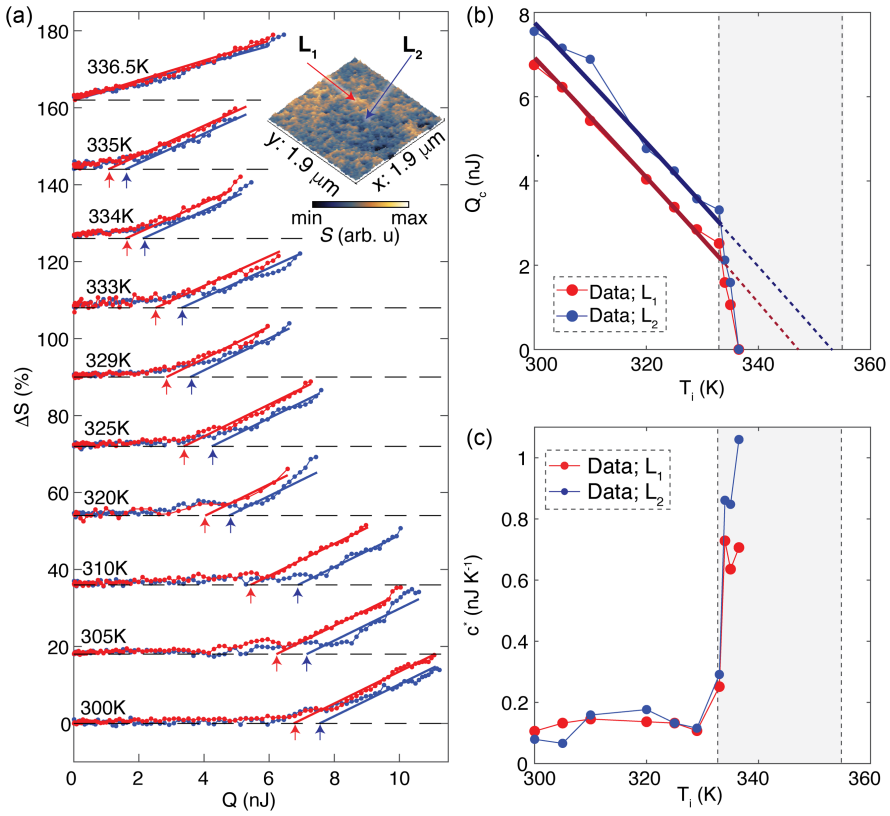

FIG. 2. Spatially resolved and temperature dependent photo-excitation energy thresholds. All data were obtained at the time delay $\Delta t = 600$ ps. (a) and (b) Raw data showing the pump-induced change of the near-field amplitude, ΔS, as a function of the applied photoexcitation energy, Q, at two locations in our film, L_1 (red) and L_2 (blue), which are separated by about 1 μm in real space (inset) for a series of initial temperatures, T_i. (a) The data are offset vertically for clarity with the dashed black line indicating $\Delta S = 0$ at each initial temperature. The red and blue solid lines are fits used to determine the thresholds, which are marked by the red and blue arrows below each trace (see main text). The inset shows an image of the examined area, obtained at $T_i = 329$ K $\Delta t = 600$ ps, $Q = 5$ nJ. (b) The photoexcitation threshold, Q_c is plotted against T_i. The solid lines are guides to the eye. The dashed lines show extrapolations. (c) The measured trend of $c^*(T_i)$. The gray shaded areas indicate a temperature range of 333–355 K, where the transition region is observed in independent resistivity measurements (Fig. S1 [19]).

measurement. Yet, our data indicate that the above-threshold transition to the metallic phase is inhomogeneous, despite the homogeneous injection of carriers. Thus, spatially uniform photoexcitation prompts inhomogeneous phase separation on the picosecond timescale, a finding which has not been explicitly shown in prior work.

To inquire into the origins of inhomogeneous optical contrasts witnessed in Fig. 1, we collected data of Q_c at a time delay of $\Delta t \cong 600$ ps, which are shown in Fig. 2. This delay is much longer than the timescales required for energy-transfer between internal, microscopic, degrees of freedom in VO_2 (for example, electron-phonon relaxation occurs in about 2–4 ps [8]). The 600 ps delay is, nevertheless, much slower than the ~10 ns timescale associated with diffusion of heat into the substrate [32]. The trends of $\Delta S(Q)$ were investigated at two representative locations, where the values of $S(Q)$ are near the extremes of high and low contrast observed in the inset of Fig. 2(a), at a series of base temperatures. Significant increases of $\Delta S(Q)$ are only observed above a critical threshold, Q_c, at each base temperature and location in Fig. 2(a). Inhomogeneous values of Q_c are documented in Fig. 2(b), consistent with Fig. 1 and prior reports [7].

To assess the role of temperature in the light-induced IMT, we examined the dependance of Q_c on the initial (equilibrium) temperature, T_i, of our sample. Starting near room temperature, a monotonic decrease of $Q_c(T_i)$ occurs in response to each increase of the initial temperature T_i at both locations in Figs. 2(a) and 2(b). To assess the observed trends of $Q_c(T_i)$, we consider values of Q_c that are obtained after photoexciting the sample at two different initial temperatures T_1 and T_2, with $T_2 > T_1$. We define the quantity $c^*(T_i) = -(\Delta Q_c/\Delta T_i)$, shown in Fig. 2(c), by normalizing the difference in the observed photoexcitation thresholds $\Delta Q_c = Q_c(T_2) - Q_c(T_1)$ to the difference of the initial temperatures $\Delta T_i = T_2 - T_1$. We note that the units of $c^*(T_i)$ are the same as the units of the heat capacity. However, the energy imparted by photoexcitation can prompt changes to many parameters apart from temperature, including changes of the structure or the itinerant

carrier density. These drives could, generally, induce phase transitions along nonthermal paths. In Ref. [19] (Supplemental Material [19], Sec. S1.1) we show that c^* is equal to the heat capacity only in the specific case that photoexcitation induces the IMT by driving VO_2 along a thermal path. Since $c^*(T_i)$ quantifies the amount that the threshold changes in response to a variation of the system's initial temperature, we call this quantity the photothermal capacity (see [19] Supplemental Material [19], Sec. 1.2 for discussion and details). Spatially uniform values of c^* are observed in Fig. 2(c), despite the inhomogeneous values of Q_c that are witnessed at the same locations in Figs. 2(a) and 2(b). We augment these data with measurements of $c^*(\Delta t)$, displayed in Supplemental Material, Fig. S1 [19], which are also found to be independent of Δt (for $4 < \Delta t < 600$ ps).

Next, we show that the IMT can onset at the same temperature at two locations where inhomogeneous photosusceptibility is also observed using nano-optical pump-probe data. Near the onset of the IMT the data shown in Figs. 2(b) and 2(c) reveal an abrupt increase (divergence) of $c^*(T_i)$ in a narrow range of temperatures (333–336.5 K). Well below the transition region, $c^*(T_i)$ remains close to the mean, around 0.15 nJ K^{-1}, for all initial temperatures. Above a temperature, $T_L = 333$ K, where the onset of the transition region is observed in resistivity measurements (Fig. S1 [19]), the data in Fig. 2(c) display an abrupt jump of $c^*(T_i)$ (approximately a ~fourfold enhancement). These observations are associated with significant decreases of Q_c observed in the temperature range of 333–336.5 K when T_i is increased in steps around only 1 K [see Figs. 2(a) and 2(b)]. Interestingly, the abrupt rise of $c^*(T_i)$ is observed at the same initial temperature $T_i = T_L = 333$ K at both representative locations that we examined in Fig. 2 despite the observation of inhomogeneous photosusceptibility that is documented in the same dataset [Fig. 2(c)]. We note that the trends of $c^*(T_i)$ documented in Fig. 2(c) resemble the divergent heat capacity (latent heat) observed at the onset of the IMT in calorimetry measurements. Similarly, the divergence of c^* indicates the onset of latent heat at T_L (see Supplemental Material [19], Sec. 1.1 for details). We establish spatially uniform values of both $c^*(T_i)$ and T_L in Figs. 2(b) and 2(c) despite clear differences in the observed values of Q_c at the same locations.

We proceed to investigate dynamics of the photoinduced response and show that the fluence threshold varies on picosecond timescales. The data in Fig. 3(a) show representative dynamics of ΔS starting from an initial temperature of $T_i = 332$ K, just below T_L, at a series of photoexcitation energies, Q. Nonmonotonic trends of $\Delta S(\Delta t)$, which depend on the applied photoexcitation energy, are observed in Fig. 3(a). At each pump energy, we observe the same three-stage process as in Fig. 1(g): (i) an initial rise of ΔS on the ~100 fs timescale (green shaded region), followed by (ii) a recovery of ΔS on picosecond timescales, with strong dependance on the photoexcitation energy (blue shaded region), and (iii) a follow-up increase of ΔS with a ~30–100 ps rise time (gray shaded region). Interestingly, observable changes of $\Delta S(Q)$ can eventually manifest at the latest pump-probe time delays, even at photoexcitation energies where $\Delta S(Q)$ exhibits a near complete recovery within 4 ps. To determine if the fluence threshold depends on the pump-probe time delay, we considered another representation of the same dataset in Fig. 3(b). At each time delay, ΔS only increases above a critical threshold of the photoexcitation energy, Q_c. Following Ref. [15] we extract values of $Q_c(\Delta t)$ by extrapolating the above threshold data to $\Delta S = 0$ with linear fits [solid blue lines in Fig. 3(b)]. Our analysis confirms time-dependent values of $Q_c(\Delta t)$. These measurements were repeated at a second location with the results, shown Figs. 3(b) and 3(c), confirming spatial inhomogeneities of $Q_c(x, \Delta t)$. The data in Figs. 2 and 3 establish the spatial-temporal evolution of $Q_c(x, \Delta t)$.

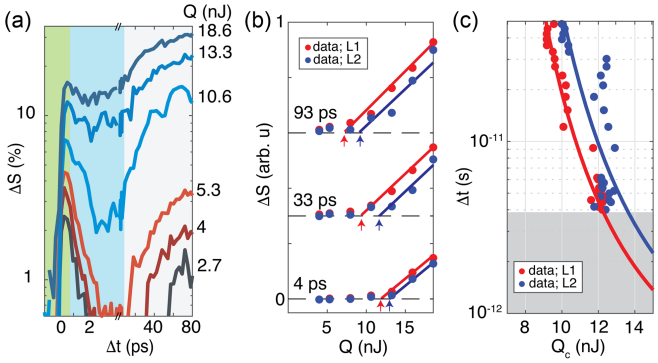

FIG. 3. Speed limits of the IMT. (a) Dynamics of ΔS obtained at a single location for a series of photo-excitation energies, Q, at $T_i = 332$ K. The values of Q used in each measurement are indicated on the right-hand side of the plot. The green, blue, and gray shaded regions mark the first, second and third stages, respectively, of the three-step response following photoexcitation described in the main text. (b) Data from (a) are plotted against Q at selected time delays. The data are vertically offset for clarity; the dashed black lines indicate $\Delta S = 0$ for each time delay. (c) The bottom axis indicates the values of $Q_c(x, \Delta t)$ extrapolated as indicated in panel (b) at each location, x, and time delay, Δt. The gray shaded region marks delays where nonthermal effects (attributed to carrier injection and relaxation—i.e., first two stages marked by the green and light blue regions in panel (b) obscure observations of Q_c. The solid red and blue lines are calculations from nucleation theory described in Sec. S1.2 [19].

In summary, our data in Figs. 1–3 establish that spatially uniform photoexcitation can prompt inhomogeneous transient metallicity in VO_2 (Fig. 1). We observed divergence of c^* at the same temperature, $T_L \approx 333$ K at two locations where an inhomogeneous photosusceptibility is also documented (Fig. 2). Last, our observations in Fig. 3 indicate Q_c does not have a characteristic "hard" single value but is better described with a "soft" series of values that depend on the pump-probe time delay.

Our principal finding is that the photosusceptibility can be enhanced within select nanoscopic regions characterized by the same critical temperature, T_L, where metallic domains can first nucleate (see Fig. 2). The observation of a soft photoexcitation threshold is reminiscent of classical nucleation theory (CNT) [33,34] where an energetic barrier, that includes both bulk and interfacial energy costs [35,36], can delay nucleation. Our observations in Fig. 3 indicate that the energetic barrier for metallic nucleation is likely inhomogeneous on mesoscopic (>100 nm) length scales. As for the microscopic origins of the inhomogeneity, the available data allow for several possibilities (see Supplemental Material [19], Sec. S1.2 for a detailed discussion). Perhaps the simplest plausible scenario is the existence of inhomogeneity on a still finer, single nanometer, length scale. Preexisting inhomogeneities could lower the energetic barrier for metallic nucleation, for example, in nanoscopic regions where a denser arrangement of pre-existing grain boundaries [12] are present. We speculate that inhomogeneities could enhance the nucleation rate of metal within select nanoscopic regions. However, any possibility that alters the energetic barrier for metallic nucleation on mesoscopic length scales could be at play. A proper explanation could require nonequilibrium treatments outside the bounds of CNT [37]. Nonetheless, the enhanced photosusceptibility revealed in Figs. 2(b) and 2(c) indicates that electronic nucleation can be enhanced in nanoscopic regions.

Here, we assessed the nucleation and growth of metallic domains during the light induced IMT. We observed inhomogeneous optical contrast prompted by spatially uniform photoexcitation, indicating an inhomogeneous photosusceptibility of VO_2. We documented divergence of the photothermal capacity at the same temperature at two locations where inhomogeneous photosusceptibility is also observed. Finally, we showed that the photoexcitation threshold varies on both nanometer spatial dimensions and picosecond timescales. We characterized the spatial-temporal evolution of the photoexcitation energy required to produce metalized VO_2 within a time Δt. Our results provide insight into the local energy cost and dynamics involved in near-threshold nucleation of the IMT. These results pave the way to efficiently drive the IMT at the smallest length scales, leveraging the least amount of material, with the lowest energy cost and highest operation speed. These attributes are desired in emerging technologies including neuromorphic computers [38–42] and smart windows [43–45].

We thank Andrea Cavalleri, Xiaoyang Zhu, and Amel Derras-Chouk for helpful discussions. This research was funded through the U.S. National Science Foundation (NSF) Materials Research Science and Engineering Centers (Grants No. DMR-2011738 and No. NSF-DMR 2210186). R. D. A. acknowledges support from the U.S. National Science Foundation Grant No. DMR-1810310. D. N. B. is Moore Investigator in Quantum Materials EPIQS GBMF9455 and the Vannevar Bush Faculty Fellow ONR-VB: N00014-19-1-2630.

*Corresponding author: ajs01123@umd.edu
†Present address: Department of Physics, University of Maryland, College Park, Maryland 20740, USA.

[1] A. Cavalleri, C. Tóth, C. W. Siders, J. A. Squier, F. Ráksi, P. Forget, and J. C. Kieffer, Phys. Rev. Lett. **87**, 237401 (2001).
[2] D. J. Hilton, R. P. Prasankumar, S. Fourmaux, A. Cavalleri, D. Brassard, M. A. El Khakani, J. C. Kieffer, A. J. Taylor, and R. D. Averitt, Phys. Rev. Lett. **99**, 226401 (2007).
[3] S. Wall *et al.*, Science **362**, 572 (2018).
[4] A. Cavalleri, T. Dekorsy, H. H. W. Chong, J. C. Kieffer, and R. W. Schoenlein, Phys. Rev. B **70**, 161102(R) (2004).
[5] A. Cavalleri, H. H. W. Chong, S. Fourmaux, T. E. Glover, P. A. Heimann, J. C. Kieffer, B. S. Mun, H. A. Padmore, and R. W. Schoenlein, Phys. Rev. B **69**, 153106 (2004).
[6] B. T. O'Callahan, A. C. Jones, J. Hyung Park, D. H. Cobden, J. M. Atkin, and M. B. Raschke, Nat. Commun. **6**, 6849 (2015).
[7] S. A. Dönges, O. Khatib, B. T. O'Callahan, J. M. Atkin, J. H. Park, D. Cobden, and M. B. Raschke, Nano Lett. **16**, 3029 (2016).
[8] M. Liu *et al.*, Nature (London) **487**, 345 (2012).
[9] M. H. Michael, M. Först, D. Nicoletti, Sheikh Rubaiat Ul Haque, Y. Zhang, A. Cavalleri, R. D. Averitt, D. Podolsky, and E. Demler, Phys. Rev. B **105**, 174301 (2022).
[10] D. Bachmann Maja *et al.*, Science **366**, 221 (2019).
[11] M. A. Huber, M. Plankl, M. Eisele, R. E. Marvel, F. Sandner, T. Korn, C. Schüller, R. F. Haglund, R. Huber, and T. L. Cocker, Nano Lett. **16**, 1421 (2016).
[12] A. J. Sternbach *et al.*, Nano Lett. **21**, 9052 (2021).
[13] Y. Zhu *et al.*, Sci. Rep. **6**, 21999 (2016).
[14] M. R. Otto, L. P. René de Cotret, D. A. Valverde-Chavez, K. L. Tiwari, N. Émond, M. Chaker, D. G. Cooke, and B. J. Siwick, Proc. Natl. Acad. Sci. U.S.A. **116**, 450 (2019).
[15] C. Kübler, H. Ehrke, R. Huber, R. Lopez, A. Halabica, R. F. Haglund, and A. Leitenstorfer, Phys. Rev. Lett. **99**, 116401 (2007).
[16] A. Pashkin, C. Kübler, H. Ehrke, R. Lopez, A. Halabica, R. F. Haglund, R. Huber, and A. Leitenstorfer, Phys. Rev. B **83**, 195120 (2011).
[17] D. Wegkamp *et al.*, Phys. Rev. Lett. **113**, 216401 (2014).
[18] A. J. Sternbach *et al.*, Opt. Express **25**, 28589 (2017).
[19] See Supplemental Material at http://link.aps.org/supplemental/10.1103/PhysRevLett.132.186903, which includes Refs. [20–27], for additional information about the experimental methods, supplemental data, and analysis.
[20] D. Lee *et al.*, Science **362**, 1037 (2018).
[21] J. C. Fisher, J. Appl. Phys. **19**, 1062 (1948).
[22] R. P. Sear, J. Phys. Condens. Matter **19**, 033101 (2007).
[23] A. Cavalleri, H. H. W. Chong, S. Fourmaux, T. E. Glover, P. A. Heimann, J. C. Kieffer, B. S. Mun, H. A. Padmore, and R. W. Schoenlein, Phys. Rev. B **69**, 153106 (2004).

[24] C.-Y. Kim, T. Slusar, J. Cho, and H.-T. Kim, ACS Appl. Electron. Mater. **3**, 605 (2021).
[25] X. Chen *et al.*, ACS Photonics **7**, 687 (2020).
[26] M. M. Qazilbash *et al.*, Science **318**, 1750 (2007).
[27] A. C. Jones, S. Berweger, J. Wei, D. Cobden, and M. B. Raschke, Nano Lett. **10**, 1574 (2010).
[28] A. S. McLeod *et al.*, Nat. Phys. **13**, 80 (2017).
[29] M. M. Qazilbash *et al.*, Science **318**, 1750 (2007).
[30] A. C. Jones, S. Berweger, J. Wei, D. Cobden, and M. B. Raschke, Nano Lett. **10**, 1574 (2010).
[31] J. M. Atkin, S. Berweger, A. C. Jones, and M. B. Raschke, Adv. Phys. **61**, 745 (2012).
[32] S. Lysenko, A. Rúa, V. Vikhnin, F. Fernández, and H. Liu, Phys. Rev. B **76**, 035104 (2007).
[33] R. Lopez, T. E. Haynes, L. A. Boatner, L. C. Feldman, and R. F. Haglund, Phys. Rev. B **65**, 224113 (2002).
[34] J. C. Fisher, J. Appl. Phys. **19**, 1062 (1948).
[35] D. Lee *et al.*, Science **362**, 1037 (2018).
[36] J. Wu, Q. Gu, B. S. Guiton, N. P. de Leon, L. Ouyang, and H. Park, Nano Lett. **6**, 2313 (2006).
[37] A. Verma *et al.*, arXiv:2304.02149.
[38] A. Sood *et al.*, Science **373**, 352 (2021).
[39] J. del Valle *et al.*, Nature (London) **569**, 388 (2019).
[40] J. del Valle *et al.*, Science **373**, 907 (2021).
[41] R. Yuan *et al.*, Nat. Commun. **13**, 3973 (2022).
[42] G. Li *et al.*, Nat. Commun. **13**, 1729 (2022).
[43] Y. Qiu, D.-X. Yan, Q.-Y. Feng, X.-J. Li, L. Zhang, G.-H. Qiu, and J.-N. Li, Opt. Express **30**, 26544 (2022).
[44] T. D. Vu, H. Xie, S. Wang, J. Hu, X. Zeng, and Y. Long, Mater. Today Energy **26**, 100978 (2022).
[45] Z. Cheng, R. Wang, Y. Cao, Z. Cai, Z. Zhang, and Y. Huang, Adv. Funct. Mater. **32**, 2205160 (2022).